

Performance comparison of a 9-kW magnetically shielded Hall thruster operating on xenon and krypton

Cite as: J. Appl. Phys. **130**, 163306 (2021); <https://doi.org/10.1063/5.0066849>

Submitted: 12 August 2021 • Accepted: 09 October 2021 • Published Online: 28 October 2021

 L. L. Su and  B. A. Jorns



View Online



Export Citation



CrossMark



Webinar
Quantum Material Characterization
for Streamlined Qubit Development



Register now

Performance comparison of a 9-kW magnetically shielded Hall thruster operating on xenon and krypton

Cite as: J. Appl. Phys. **130**, 163306 (2021); doi: [10.1063/5.0066849](https://doi.org/10.1063/5.0066849)

Submitted: 12 August 2021 · Accepted: 9 October 2021 ·

Published Online: 28 October 2021



View Online



Export Citation



CrossMark

L. L. Su^{a)} and B. A. Jorns

AFFILIATIONS

Department of Aerospace Engineering, University of Michigan, Ann Arbor, Michigan 48109, USA

Note: This paper is part of the Special Topic on Physics of Electric Propulsion.

^{a)}**Author to whom correspondence should be addressed:** leannesu@umich.edu

ABSTRACT

The performance of a 9-kW class magnetically shielded Hall thruster operating on xenon and krypton propellants is experimentally characterized. Thrust and efficiency measurements performed at discharge powers ranging from 4.5 to 9 kW indicate that the anode efficiency of krypton is 9%–18% lower than that of xenon. This difference is comparable to previous measurements reported for unshielded Hall thrusters, although it is found that unlike in previous studies, the efficiency ratio widens with increasing discharge voltage. Far-field probes are employed to measure the contributions to anode efficiency at conditions of 4.5 and 6 kW. These results indicate that mass utilization has the largest impact on the difference in performance between xenon and krypton. Assuming this mass utilization remains the dominant driver at higher voltages, it is proposed that the higher electron temperature of shielded thrusters along channel centerline coupled with the nonlinearity of the ionization cross section may explain why the efficiency gap widens with increasing voltage for shielded thrusters. The results are discussed in the context of optimizing magnetically shielded Hall thrusters for improved performance on krypton propellant.

Published under an exclusive license by AIP Publishing. <https://doi.org/10.1063/5.0066849>

I. INTRODUCTION

The advent of magnetic shielding on Hall thrusters, a technique that reduces channel erosion by shaping the magnetic fields, has greatly extended the lifetimes of these devices compared to unshielded Hall thrusters.^{1,2} These increased lifetimes enable longer-duration missions, which in turn require more propellant. While xenon has historically been the propellant of choice for Hall thrusters due to its low ionization energy and high mass, fluctuations in price and availability that stem from the widespread demand for this gas in other industries can pose a risk for longer, more ambitious missions.^{3–6} Indeed, it was recently shown that the required xenon propellant for next-generation deep-space missions proposed by NASA could potentially exceed 10% of the annual worldwide production.⁵ In light of these limitations, krypton has been proposed as an alternative propellant. It is ten times more abundant in the atmosphere⁷ and up to an order of magnitude lower in cost.^{4,8} These advantages have led to the adoption of

krypton in the Hall thrusters on the Starlink satellite constellation currently in operation by SpaceX.

While krypton has operational benefits, there remain two major limitations for adopting this propellant, particularly for deep-space applications. The first is its storage density, which is a third that of xenon at the same pressures and temperatures.^{6,9} This limitation can lead to prohibitively large storage tanks for missions with larger propellant requirements, though it could in part be overcome by storing at higher pressures. The second challenge stems from performance, as previous studies have shown that the anode efficiency of Hall thrusters operating on krypton is 5%–15% lower than that of xenon at the same conditions.^{10–16} This difference in efficiency has primarily been attributed to the lower mass utilization of krypton.^{12–17} In practice, this reduction can be a major mission driver, especially for high-power missions where overall system efficiency is critical.

One major caveat regarding previous comparisons of xenon and krypton performance is that they were conducted on Hall

thrusters with a more traditional “unshielded” magnetic field configuration. Magnetic shielding is achieved with a specially designed field shape that ensures low electron temperatures and high electric potentials at the walls of the thruster discharge channel.^{1,2} While this geometry has the benefit of reducing erosion-causing energetic ion flux to the walls, it also can lead to changes in the distribution of the plasma state and, therefore, thruster performance. For example, magnetically shielded (MS) thrusters exhibit higher electron temperatures along centerline and a downstream shift of the ion acceleration region compared to unshielded (US) thrusters.^{2,18} Similarly, a previous comparison of US and MS operation on the H6, a 6-kW class Hall thruster, indicated that efficiency modes such as voltage and current utilization increased when changing from US to MS thrusters, while other efficiency terms like mass utilization and divergence decreased, leading to a total 1.5% decrease in anode efficiency.¹⁸

The change in plasma configuration that results from the differences in the US and MS designs may in turn lead to differences in the performance gap between krypton and xenon. For example, given the higher electron temperatures along centerline in MS thrusters, we may expect the mass utilization for krypton to be higher, thus reducing the efficiency loss. To date, however, it has yet to be shown experimentally how shielding may impact the transition from xenon to krypton. In light of the increasing use of magnetically shielded Hall thrusters and the potential advantages afforded by krypton operation, there is a pressing need for this type of detailed investigation.

The goal of this study is to compare the operation of a magnetically shielded Hall thruster with xenon and krypton propellants and to identify the key drivers of performance. To this end, this paper is organized in the following way. In Sec. II, we outline the metrics we use to characterize thruster performance. In Sec. III, we

describe the experimental setup, including the thruster and facility used for these tests. This section also includes a description of the diagnostics and methodology used to collect and process data throughout the experiment. In Sec. IV, we present the results of our study, including a summary of measured efficiencies, thrusts, and specific impulses for both xenon and krypton at all operating conditions. In Sec. V, we discuss the potential reasons for the gap between xenon and krypton performance on a shielded thruster and draw comparisons to unshielded thrusters. We explore possible physical explanations for why this change exists as well as potential mitigation strategies for future krypton-operated magnetically shielded Hall thrusters.

II. METRICS FOR EVALUATING THRUSTER PERFORMANCE

In this section, we present an overview of the key metrics for evaluating Hall thruster performance. This provides a common framework for contrasting the operation of xenon and krypton. To this end, we show in Fig. 1 schematically the principle of operation of a Hall thruster and the various parameters used to evaluate the efficiency breakdown. In this axisymmetric device, a discharge voltage, V_d , is established between the anode and cathode, generating a discharge current, I_d , within the channel and an electric field that points axially downstream (Fig. 1). A radial magnetic field is applied orthogonal to this electric field within the channel. Neutrals that are injected through the anode become ionized through collisions with electrons supplied by the cathode. Due to the mass differential between electrons and ions, the ions are largely unmagnetized and accelerated out of the channel by the electric field. The electrons, however, are strongly magnetized and confined to an azimuthal $E \times B$ drift within the channel. The

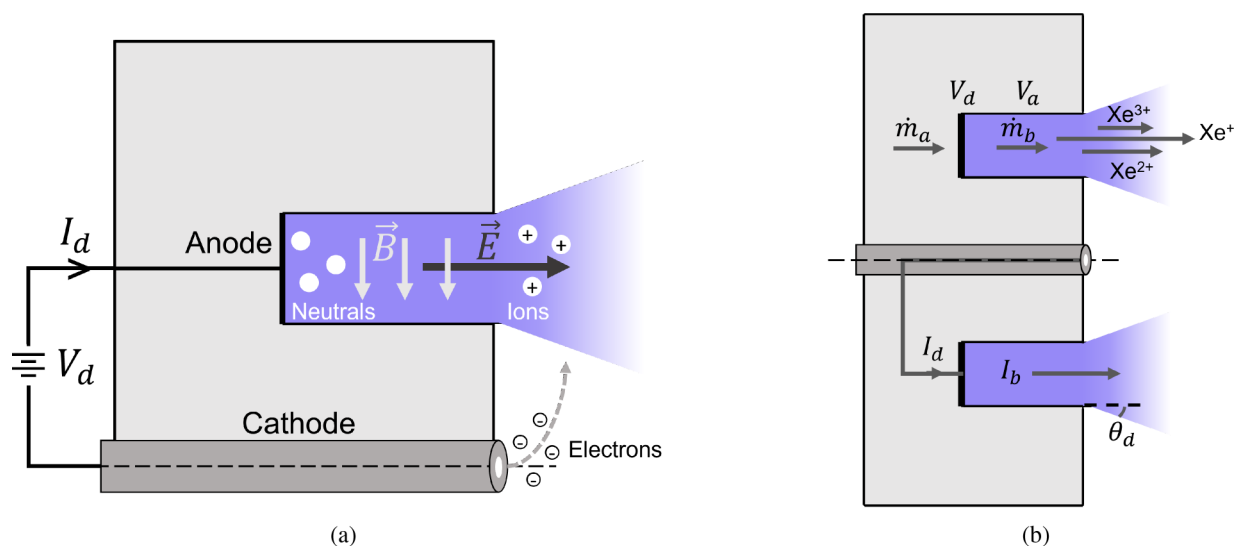


FIG. 1. Cross section schematic view of a Hall thruster with (a) one channel illustrating the principle of operation and (b) a full cross section highlighting relevant plasma parameters that impact efficiency.

plume is neutralized downstream by the injection of additional electrons from the cathode.

In terms of global performance metrics for this system, we consider thrust, T , a measure of net axial force generated; specific impulse, I_{sp} , the normalized exhaust velocity; and the anode efficiency, η_a , a metric that indicates the conversion of electrical power into directed kinetic energy. The thrust and specific impulse are related through the standard form,

$$I_{sp} = \frac{T}{(\dot{m}g_0)}, \quad (1)$$

where \dot{m} is the total mass flow rate and g_0 is the gravitational acceleration. The anode efficiency in turn is defined as

$$\eta_a = \frac{T^2}{2\dot{m}_a P_d}, \quad (2)$$

where \dot{m}_a is the mass flow through the anode and P_d is the discharge power, calculated from $P_d = V_d I_d$. The anode efficiency neglects losses from the cathode flow and magnet power, thus allowing us to more directly evaluate the efficiency of a thruster isolated from the larger system.

There are a number of non-ideal factors [Fig. 1(b)] that impact the overall anode efficiency. We quantify these contributions following the Hall thruster model developed by Hofer *et al.*,^{19–22} which defines the anode efficiency as the product of five terms,

$$\eta_a = \eta_b \eta_v \eta_d \eta_q \eta_m, \quad (3)$$

where η_b is the current utilization efficiency, η_v is the voltage utilization efficiency, η_d is the plume divergence efficiency, η_q is the charge utilization efficiency, and η_m is the mass utilization efficiency. In particular, we have the following definitions:

- **Current utilization efficiency:** The ratio of ion current contained in the plume to the discharge current is defined as

$$\eta_b = \frac{I_b}{I_d}, \quad (4)$$

where I_b is the ion beam current. This efficiency captures the fact that not all of the discharge current is converted to ions as some is carried by electrons from the cathode to the anode.

- **Voltage utilization efficiency:** The conversion of applied voltage into ion velocity is defined as

$$\eta_v = \frac{V_a}{V_d}, \quad (5)$$

where V_a is the average acceleration voltage, the potential drop through which ions are accelerated in the channel. This efficiency represents the loss in discharge voltage that is not available for accelerating ions. For example, some fraction of this potential is required to draw electrons out of the cathode.

- **Plume divergence efficiency:** The decrease in axially directed momentum from the divergence of the ion beam is defined as

$$\eta_d = (\cos \theta_d)^2, \quad (6)$$

where θ_d is the angle of plume divergence from channel centerline. This efficiency captures the fact that radially directed momentum does not contribute to thrust.

- **Charge utilization efficiency:** The decrease in efficiency from multiply charged ions in the beam is defined as

$$\eta_q = \frac{\left(\sum_i \frac{\Omega_i}{\sqrt{Z_i}}\right)^2}{\sum_i \frac{\Omega_i}{Z_i}}, \quad (7)$$

where Z_i is the charge state of the i th ion species and $\Omega_i = \frac{I_i}{I_d}$ is the current fraction of the i th ion species where I_i is the total contribution to current from a given ion species. This efficiency encapsulates the presence of multiply charged species in the plume.

- **Mass utilization efficiency:** The conversion of neutral mass flux into ion mass flux is defined as

$$\eta_m = \frac{\dot{m}_b}{\dot{m}_a} = \frac{m_i I_b}{q \sum_i \frac{\Omega_i}{Z_i}} = \xi \eta_b \sum_i \frac{\Omega_i}{Z_i}, \quad (8)$$

where \dot{m}_a is the neutral anode mass flow rate, \dot{m}_b is the ion beam mass flow rate, a measure of how many ions are flowing into the beam, m_i is the ion mass, q is the elementary charge, and $\xi = \frac{I_d m_i}{q \dot{m}_a}$ is a value defined as the exchange ratio. This efficiency represents the fact that not all neutrals are ionized and, therefore, not accelerated out by the electric field.

We can use this model for the breakdown of anode efficiency to identify what specific processes within the thruster are primarily contributing to performance losses. By measuring each of these efficiency components, we can also compare the anode efficiency calculated by taking the product of all five modes, $\eta_{a,probe}$, to the anode efficiency calculated with the thrust, anode mass flow rate, and discharge power, $\eta_{a,thrust}$. With our metrics for evaluating performance defined, we describe Sec. III, an experimental setup including the test article, thrust stand, probe diagnostics, and techniques for characterizing the global metrics as well as efficiency contributions for a shielded Hall thruster.

III. EXPERIMENTAL SETUP

In this section, we describe the test article and facility used for our experiment, our chosen operating conditions, the diagnostics used to collect data of the plasma parameters, and the data analysis methods we employed to calculate our performance metrics.

A. Thruster and facility

For this study, we used the H9, a 9-kW class magnetically shielded Hall thruster developed in partnership between the University of Michigan (UM), Jet Propulsion Laboratory (JPL), and the Air Force Research Laboratory (AFRL).^{23,24} Figure 2 shows the H9 operating on both xenon and krypton propellants. The H9 employs a centrally mounted LaB6 cathode²⁵ operating at a fixed

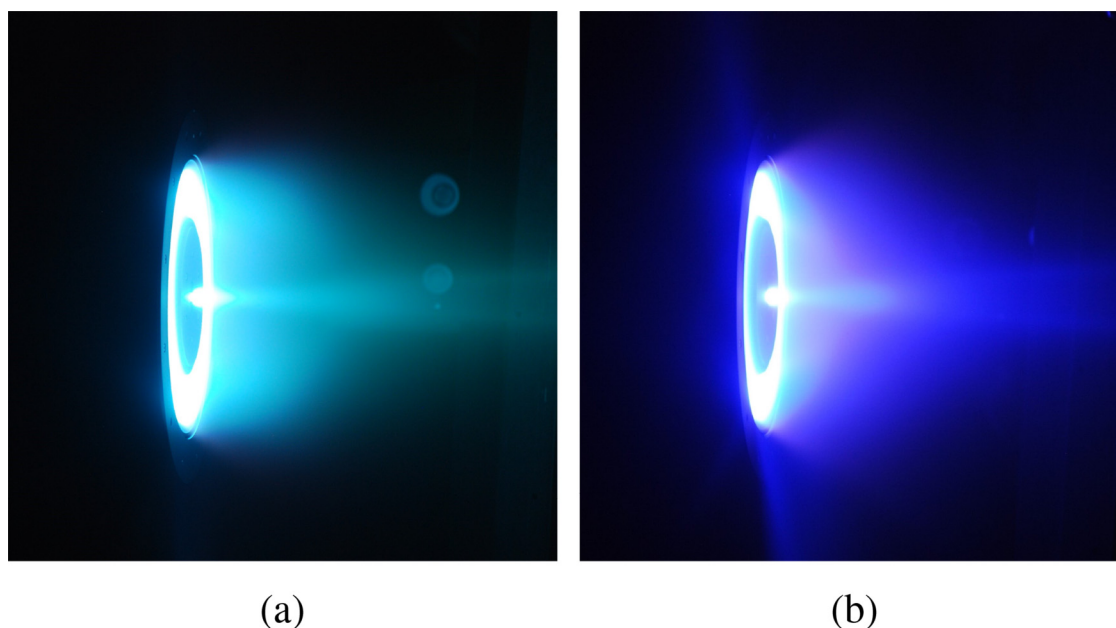


FIG. 2. The H9, a 9-kW class magnetically shielded Hall thruster, operating at 300 V and 15 A on (a) xenon and (b) krypton.

7% cathode flow fraction. This cathode was electrically connected to the thruster body and isolated from facility ground.²⁶

All tests were conducted at the University of Michigan in the Large Vacuum Test Facility (LVTF), a chamber 6 m in diameter and 9 m in length capable of pumping ~ 500 kl/s of xenon and ~ 600 kl/s of krypton during high-power thruster operation.²⁷ The thruster was operated on xenon and krypton at background pressures of 4.8–5.8 Xe- μ Torr and 4.5–5.8 Kr- μ Torr. Pressures in the

chamber were measured with a Stabil ion gauge calibrated for xenon, mounted 1 m away from the thruster in the thruster exit plane and pointing downstream as shown in Fig. 3 per industry best practices.²⁸

Table I shows the operating conditions we considered for this study. The magnetic field shape remained the same in each case, but the magnitudes, which are referenced to the nominal magnitude at the 4.5-kW condition, were adjusted to minimize oscillations and discharge current. We note that while we made global performance measurements (thrust, specific impulse, and efficiency) at all operating conditions, we only collected probe data at the 300 V and 15 A, 300 V and 20 A, and 400 V and 15 A conditions. This stemmed from concerns about thruster stability at higher powers where we observed discharge current oscillations over 160%–210% when the thruster was operated with krypton. The time to generate a complete set of probe data under these conditions was judged to be prohibitively long and unsafe for thruster health.

B. Diagnostics

We used a null-type inverted pendulum thrust stand to collect thrust data and evaluate anode efficiency at all conditions. The thrust stand employed double-ended pivot bearings and a series of weights for calibration.^{29,30} The thrust stand has an uncertainty of ± 1 –3 mN and a resolution of ~ 1 mN.

To evaluate the plume properties that contribute to the terms in the efficiency model [Eq. (3)], we used a probe suite consisting of a retarding potential analyzer (RPA), emissive probe (EP), Langmuir probe (LP), Faraday probe (FP), and $E \times B$ probe. The RPA, EP, LP, and FP were mounted on an azimuthal probe arm

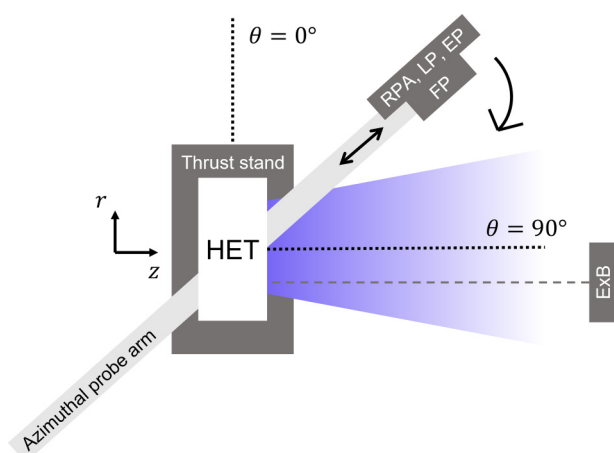


FIG. 3. Notional overhead view of thruster, thrust stand, and probe suite in the vacuum chamber.

TABLE I. Operating conditions and base pressures. Note that probe data was only collected for the first three conditions.

Voltage (V)	Current (A)	Power (kW)	Xe anode flow rate (mg/s, SCCM)	Kr anode flow rate (mg/s, SCCM)	Xe pressure (μ Torr)	Kr pressure (μ Torr)	Xe B-field ratio (%)	Kr B-field ratio (%)
300	15	4.5	14.8, 165	11.8, 207	4.8	4.6	100	100
300	20	6	18.5, 206	15.3, 268	5.8	5.8	100	87.5
400	15	6	15.4, 172	11.5, 201	5.0	4.5	100	112.5
500	15	7.5	16.1, 179	12.0, 209	5.3	4.7	100	112.5
600	15	9	15.4, 171	12.5, 218	5.4	4.9	100	112.5

with an axis of rotation above the exit plane of the thruster (Fig. 3). These probes yielded data at a location $10.25 D_T$ thruster diameters (D_T) downstream, with the FP taking additional sweeps at 9.25 and $8.25 D_T$. The RPA, EP, and LP each provided a single trace at 90° , directly facing the centerline of the thruster, while the FP was swept from 0° to 180° with a resolution of $\sim 1^\circ$. The $E \times B$ probe was mounted $\sim 10.5 D_T$ downstream of the thruster and aligned to the channel centerline.

The RPA we employed had four grids and a collector inside with a 6.45 cm^2 aperture. Both the primary and secondary electron suppression grids were set to -30 V , and the ion selection grid was swept from 0 to $\sim 2 \times$ the discharge voltage. The emissive probe we used consisted of a 1 mm length thoriated tungsten filament loop, heated to thermionic emission such that the probe potential approached the plasma potential. We employed a Langmuir probe that was comprised of a 4 mm length tungsten wire routed through a ceramic tube. This probe was biased from -5 to 15 V . The Faraday probe used to measure ion saturation current had a 1.74 cm inner diameter molybdenum collector and 2.38 cm outer diameter molybdenum guard ring, with a 0.05 cm gap between them, and was biased to -30 V for probe sweeps. The $E \times B$ probe had an entrance aperture 1.6 mm in diameter, an entrance collimator 7.5 cm long, an exit collimator 15 cm long, and electrical plates spaced 0.97 cm apart. The peak magnetic field was 0.16 T in the center of the probe. We swept the applied bias voltage to the plates from 0 to 70 V to fully map the charge states in the plume.

C. Data analysis

In this section, we describe how we used the telemetry from the probes to estimate the plasma parameters necessary for evaluating the efficiency terms outlined in Sec. II. Specifically, we describe our methodologies for estimating the acceleration voltage, charge fractions, divergence angle, and beam current.

1. Acceleration voltage

We defined the acceleration voltage in Eq. (5) as the most probable ion kinetic energy in the far-field plume. To infer this value, we first differentiated the current-voltage trace from the RPA diagnostic. This yielded an estimate for the distribution of ion energy per unit charge (Fig. 4), the peak of which corresponds to the most probable ion energy, V_{RPA} . As the RPA was biased with respect to facility ground, we converted this most probable value to an estimation of acceleration voltage by subtracting the

local plasma potential,

$$V_a = V_{RPA} - \phi_p. \quad (9)$$

To determine the plasma potential, ϕ_p , we used the emissive and Langmuir probes. The floating potential, ϕ_f , inferred from the heated emissive probe, yielded this plasma parameter with a temperature correction, $\phi_p = \phi_f + \alpha T_e$, where α is a scalar factor and T_e is the electron temperature. This correction assumes a Maxwellian electron energy distribution and accounts for space charge effects, with values of α ranging from 0 to 1.5 .³¹ We evaluated both limits of α to provide bounds of ϕ_p to average over. To infer the electron temperature, we used the inverse slope of the current-voltage Langmuir probe trace as plotted on a log-linear scale.³²

We used a bootstrapping method to estimate the error in V_{RPA} ,³³ sampling a subset of the raw RPA trace and performing the same method as described above for the most probable voltage. This process was repeated a thousand times and the standard deviation in the resultant values of V_{RPA} was taken to be the uncertainty of the most probable voltage. This uncertainty was compounded with the uncertainty stemming from the variation in

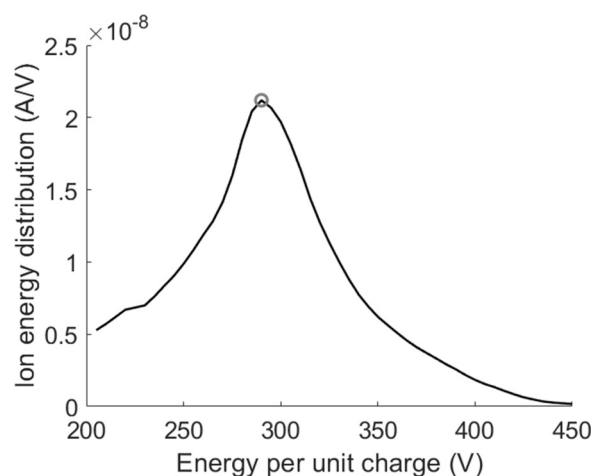


FIG. 4. Distribution of ion energy per unit charge inferred from the RPA at an operating condition of 300 V and 15 A on krypton and at a location $10.25 D_T$ radially downstream from the thruster. The most probable energy, V_{RPA} , is indicated with a gray circle. Potentials are referenced with respect to facility ground.

the correctional factor α to yield a total estimate for error in the reported values of V_a and η_v .

2. Charge fractions

We show in Fig. 5 an example of a typical trace inferred from the $E \times B$ probe. The multiple peaks correspond to the different charge states in the plasma. In order to infer the relative fraction, Ω_i , of each of these species, we followed the approach outlined in Ref. 34 by progressively fitting dual Gaussian distributions for each of the species found in the raw trace. This previous work also showed that the choice of a dual Gaussian functional form better captures the high-velocity tails frequently exhibited by Hall thruster ion velocity distributions. Indeed, we found that other fit functions that have been proposed previously, such as a single Gaussian, yielded unphysical results for the charge state. In our procedure, we first fit to the largest peak, assuming it to be representative of the singly charged species, then subtracted off this fitted curve. We repeated the process for higher charge states up to quadruply charged ions. Figure 5 shows examples of the fits from this process as well as the residuals, defined as the difference between the raw trace and the fits. We estimated uncorrected charge fractions from these fits by integrating the area of each peak and comparing it to the total integrated area under the curve.

The presence of background neutrals necessitates the consideration of charge-exchange (CEX) collisions in correcting the charge fractions. This was done by modifying the integrated current and density with a term $(j/j_0)_i$ for the i th ion species. This factor corrects the raw value of each charge species $\Omega_{i,raw}$ as described in Refs. 35 and 36,

$$\Omega_i = \frac{\Omega_{i,raw}(j/j_0)_i^{-1}}{\sum_k (\Omega_{k,raw}(j/j_0)_k^{-1})}, \quad (10)$$

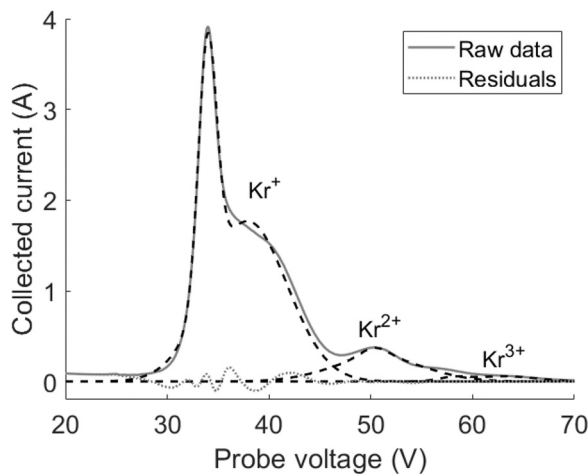


FIG. 5. $E \times B$ trace with dual Gaussian fits (dotted black lines) for the singly, doubly, and triply charged ions at an operating condition of 300 V and 15 A for krypton and at a location $\sim 10.5 D_T$ radially downstream from the thruster. Note that the quadruply charged ion species is too small to be resolved on the plot.

where the summation over k in the denominator is the total area under the fitted curves. Each correction factor is calculated as

$$(j/j_0)_i = \exp(-n_0 \sigma_i z), \quad (11)$$

where n_0 is the background neutral density, σ_i is the cross-sectional area for the i th ion species, and z is the distance of the $E \times B$ probe from the exit plane. We calculated n_0 from our measurements of chamber pressure in the exit plane shown in Table I, with an uncertainty in our ion gauge pressure measurement of 10%. The expressions for the cross-sectional areas of the i th charge state of xenon are taken from Ref. 37,

$$\sigma_1|_{Xe} = (87.3 - 13.6 \log(V_1)) \times 10^{-20}, \quad (12)$$

$$\sigma_2|_{Xe} = (45.7 - 8.9 \log(2V_2)) \times 10^{-20}, \quad (13)$$

$$\sigma_3|_{Xe} = (16.9 - 3.0 \log(3V_3)) \times 10^{-20}, \quad (14)$$

where V_i is the voltage through which the i th ion species is accelerated. For our analysis, we assumed that all values of V_i are equivalent to the calculated acceleration voltage V_a . The ratio of Xe^{4+} was typically small enough (less than $\sim 5\%$) such that we neglected the correctional factor for this state.

For krypton, we used the cross-sectional areas listed in Ref. 38 for the first two charge states,

$$\sigma_1|_{Kr} = (80.7 - 14.7 \log(V_1)) \times 10^{-20}, \quad (15)$$

$$\sigma_2|_{Kr} = (44.6 - 9.8 \log(2V_2)) \times 10^{-20}, \quad (16)$$

where we once again used the acceleration voltage V_a for each species. As there were no tabulated data for the cross-sectional area of Kr^{3+} , we approximated the expression using Eq. (14). This was deemed acceptable as the constants for the first and second charge states of xenon and krypton are within 10% of each other; additionally, because the ratio of Kr^{3+} is low overall (less than $\sim 4\%$), the impact of this error is minimal. We assumed that $(j/j_0)_4 = 1$ for krypton as we did for xenon. We quantified uncertainty in the final charge species by accounting for two sources of error following the methodology in Ref. 36. First, we quantified the error from the fit by integrating under the area of the residual curve for each charge state. Second, we quantified the error in the CEX correction by propagating the uncertainty of the neutral density due to the pressure measurement.

3. Divergence angle, beam current, and beam ion mass flow rate

We employed current density estimates from the Faraday probe to infer both the current and divergence utilization efficiencies. Before making these assessments, however, it was necessary to make a number of corrections to the raw telemetry from the FP. These are described in detail in Ref. 39 and include a correctional factor, κ_G , to account for the probe geometry, as well as a coefficient, κ_{SEE} , that accounts for the secondary electron emission (SEE)

TABLE II. Secondary electron emission coefficients for charge states 1–4 of xenon and krypton.

Gas	γ_1	γ_2	γ_3	γ_4
Xe	0.021	0.199	0.697	1.393
Kr	0.069	0.296	0.859	1.889

current induced by incident ions. The corrected ion current density is thus given by

$$j = \frac{I_{FP}}{A_C + \kappa_G} \kappa_{SEE}, \tag{17}$$

where j is the current density of the plume, I_{FP} is the current measured by the collector, and A_C is the area of the FP collector. For our analysis, we adopted the same formula for geometric correction factor as given in Ref. 39, yielding a value of $\kappa_G = 7.7 \times 10^{-6} \text{ m}^2$. We similarly used the same SEE correction factor from this reference for the first three charge states of xenon. However, for our work, we also included the fourth charge state of xenon and introduced coefficients for correcting krypton SEE up to the fourth charge state. To this end, we note that the SEE correctional factors are defined as

$$\kappa_{SEE} = \frac{1}{1 + \sum_i \frac{\Omega_i \gamma_i}{Z_i}}, \tag{18}$$

where the charge fraction Ω_i is inferred from the $E \times B$ probe and γ_i is the SEE coefficient of the i th charge state.

Brown *et al.*'s previous work determined the values for the first and second charge states of xenon by averaging γ_i from 100 to 1000 eV with measurements of xenon impinging on molybdenum from Hagstrum.⁴⁰ For the third charge state, they used the ratio of higher to lower γ_i of tungsten from a separate study by Hagstrum,⁴¹ as these ratios were not measured for molybdenum. They assumed the same ratio between the third and the second charge state for tungsten as for molybdenum to infer a value for the third charge state of xenon impinging on molybdenum. For our work, we extended this methodology to determine the SEE coefficient for the fourth charge state of xenon. Additionally, we used the same overall method to calculate all four values of γ_i for krypton. The SEE coefficients we found from this technique are tabulated in Table II.

Armed with this formulation of corrected current density, we plot in Fig. 6 an example trace of current density as a function of angle. As this figure shows, the density is higher closer to centerline, which is where most of the beam is located. The density then decreases with angle. The periphery of the beam consists of a convolution of ions originating from the thruster as well as those born from charge-exchange collisions with background facility neutrals. As was pointed out in Ref. 42, these slow ambient ions can artificially inflate the current trace, especially in the presence of a large CEX population as there is in the wings.

In order to accurately infer the key properties of total beam current and divergence angle from these current density plots, we corrected for the CEX effect in two ways. For the divergence angle, we

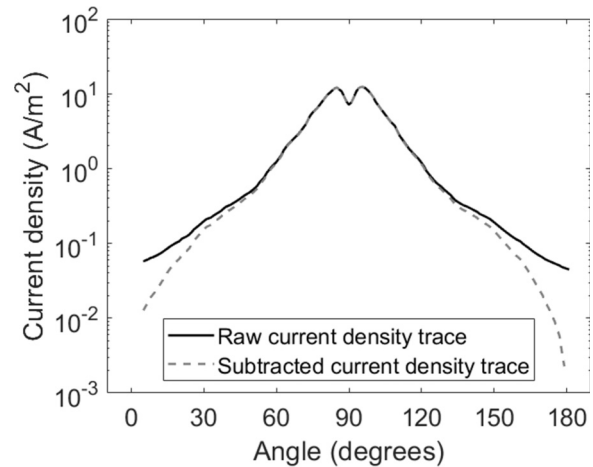


FIG. 6. Current density inferred from the Faraday probe at an operating condition of 300 V and 15 A for krypton and at a location 10.25 D_T radially downstream from the thruster. The black solid line indicates the raw current density while the gray dashed line indicates the current density with the lowest value subtracted.

used the methodology provided by Brown *et al.*³⁹ and Huang *et al.*,⁴³

$$\cos \theta_d = \frac{\int_0^{\pi/2} j(\theta) \cos \theta \sin \theta d\theta}{\int_0^{\pi/2} j(\theta) \cos \theta d\theta}, \tag{19}$$

where θ is the azimuthal location of the probe in radians where 0 is in line with the thruster exit plane (Fig. 3). Physically, this expression represents the ratio of the axially directed beam current to the total beam current. We measured the divergence angle at three locations, 8.25, 9.25, and 10.25 D_T , axially downstream from the thruster. We then applied a linear fit to the exit plane to determine the divergence angle at the thruster. We estimated error in this angle as the standard deviation of the fit parameters.

The beam current was calculated from measurements of the current density as

$$I_b = 2\pi R^2 \int_0^{\pi/2} j(\theta) \cos \theta d\theta, \tag{20}$$

where R is the distance from the thruster exit plane to the probe. Multiple methods of accounting for the impact of CEX on this beam current calculation have been proposed to date;^{34,44} however, these methods are designed to estimate the beam current at zero facility pressure. As we did not extrapolate all our other performance measurements to zero pressure, we instead adopted a method based on placing upper and lower bound estimates for the beam current calculations at the base operating pressure. The integrated value of I_b from the raw trace was treated as the upper bound for the beam current, while for the lower bound, we subtracted the value of j at the point furthest away from centerline (i.e., 0° or 180°) following Ref. 45. This was motivated by the assumption that any charge collected at this peripheral location is purely

due to ambient ions without any beam ions. Figure 6 shows an example of these “raw” and “subtracted” traces. We averaged the six estimates of beam current (an upper and lower bound at each of the three distances) to determine our average value for I_b . The error is reported as the standard deviation in these six values.

We determined the mass utilization efficiency from Eq. (8) by using the measured discharge current, beam current as determined by the FP, and ratios of charge species as determined by the $E \times B$ probe. We estimated uncertainty in this efficiency by propagating the individual sources of error from each measurement. The product of the individually calculated efficiencies was taken to be the “probe-calculated” anode efficiency, $\eta_{a,probe}$, as shown in Eq. (3), with the error from individual efficiencies again propagated forward to yield a final estimate of overall uncertainty.

IV. RESULTS

In this section, we first compare the global performance metrics calculated for xenon and krypton at each operating condition, including thrust, specific impulse, and anode efficiency. We then present the phenomenological efficiency contributions as described in Sec. II for each gas individually.

A. Trends in overall performance

Figure 7 shows the thrust, specific impulse, and anode efficiency as a function of operating condition for both xenon and krypton. These results are broadly in keeping with previous investigations into the performance of unshielded Hall thrusters on these propellants.^{10–15,18}

1. Thrust

We see that the thrust [Fig. 7(a)] increases linearly with power for both gases, with xenon producing ~ 60 – 100 mN more than krypton at each power level. The general trend of increasing thrust with power results from the increasing acceleration voltage (and, therefore, ion exhaust velocity) while maintaining an approximately constant mass flow rate. The higher thrust levels of xenon relative to krypton, which has been observed in previous comparison studies of unshielded thrusters,^{10,11,14,16} can be understood in light of the difference in their masses. For both gases, the 20 A condition exhibits higher thrust than the 15 A condition at 6 kW. This result stems from the fact that the acceleration voltage remains approximately constant while we increased the flow rate to achieve the higher discharge current.

2. Specific impulse

Figure 7(b) shows the specific impulse as a function of propellant and power. We see that in both cases, this value monotonically increases with power, consistent with previous parametric studies performed on unshielded thrusters.^{10,11,14,15,19} This trend is due to the fact that as the acceleration voltage increases with discharge voltage, the ions are accelerated to a higher effective exhaust velocity (cf. Ref. 22). Notably, the specific impulse at the 20 A condition is higher for both gases in comparison to the 15 A condition at the same discharge voltage, implying that thruster efficiency increases with current at a fixed voltage. However, the specific impulses at

300 V, 20 A are lower than those at 400 V, 15 A due to the primary scaling of specific impulse with acceleration voltage.

At all conditions except 9 kW (600 V and 15 A), the specific impulse of krypton is marginally higher (~ 20 – 200 s) than that of xenon. The difference in specific impulse between gases can be understood in part from the lower mass of krypton, leading to a higher velocity for a given acceleration voltage. With that said, ideally, the specific impulse ratio should scale inversely with the square root of mass. Assuming singly charged ions, an acceleration voltage equivalent to the discharge voltage, and a fully collimated beam (i.e., $\eta_q = 1$, $\eta_d = 1$, $\eta_a = 1$), the theoretical limit of specific impulse is

$$I_{sp,th} = \frac{\sqrt{2qV_d}}{\sqrt{m_i g_0}}. \quad (21)$$

This yields values of ~ 2100 – 3000 s for xenon and ~ 2700 – 3800 s for krypton.

The ratio of the measured specific impulse to the theoretical limit of specific impulse is shown in Fig. 8. We see that the specific impulse of krypton is $\sim 70\%$ of its theoretical limit while xenon is $\sim 90\%$ of its theoretical limit, suggesting that the efficiency of krypton is generally lower than that of xenon. This matches the trends shown in Fig. 7(c). In an extreme case, we see from Fig. 7(b) that at 9 kW, the specific impulse of xenon is about 80 s higher than krypton's. This suggests that the disparity in anode efficiency is sufficiently large at this condition to nullify the increase in krypton exhaust velocity that results from its smaller atomic mass. We note here that these trends showing the disparity in higher specific impulse and lower efficiency of krypton operation are not unique to the H9 and are in family with the results of previous studies on unshielded thrusters.^{10–15}

3. Anode efficiency

Figure 7(c) shows the anode efficiencies of both xenon and krypton as functions of operating condition. We see that this parameter increases with power in both cases, with anode values improving from 64.2% to 74.3% for xenon and from 52.2% to 54.8% for krypton. Since current remains fixed with the exception of the 20 A case, this trend indicates that increasing discharge voltage facilitates more efficient thrust generation. The general trend of increasing efficiency with voltage has been observed in a previous study of an unshielded thruster where the magnetic field was tailored to regulate electron current at higher discharge voltage. Ultimately, the improvements in performance with higher voltage were attributed to the increasing beam, mass, and voltage utilization efficiencies.¹⁹ We explore these individual efficiency contributions in further detail in Sec. V.

The parametric change in anode efficiency is different between the two gases. Quantitatively, this metric on xenon is higher than krypton at all conditions with a difference ranging from 9 to 18 ± 2 –3%. Qualitatively, the efficiency of xenon increases more rapidly, i.e., with a more pronounced slope, from 4.5 to 9 kW when compared to krypton. This disparity leads to a widening gap between krypton and xenon efficiency at higher voltages, a behavior that differs from what has been reported on unshielded thrusters. Most notably, while the efficiency gap on unshielded thrusters was

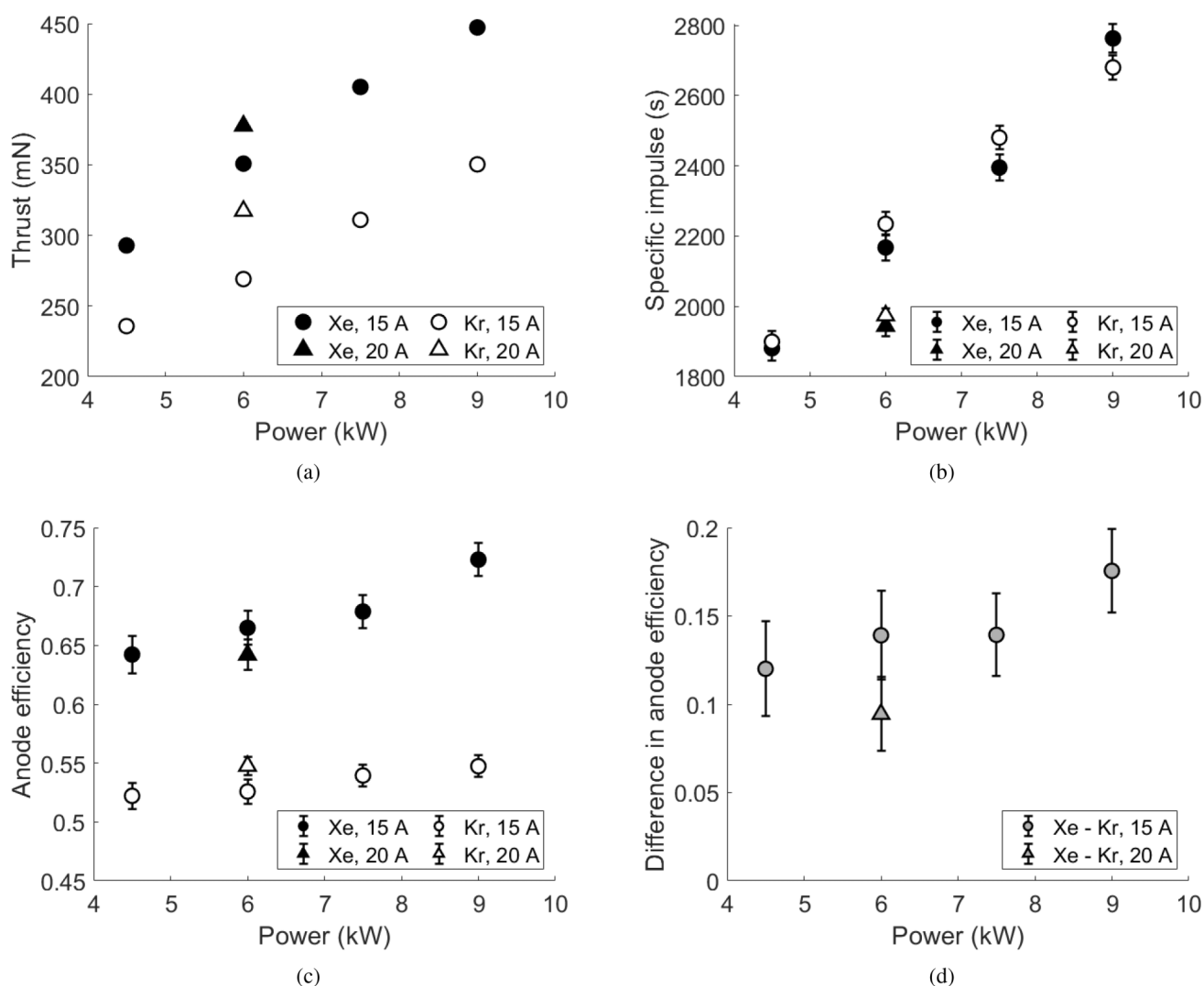


FIG. 7. (a) Thrust, (b) specific impulse, (c) anode efficiency, and (d) the difference in anode efficiency between xenon and krypton as a function of operating condition. Note that the uncertainties on Fig. 7(a) are smaller than the point sizes.

similar over a comparable voltage range (5%–15%) to the gap we report here,^{10–15} the trends in voltage differed. Specifically, the efficiency of krypton increased more rapidly with voltage than it did for xenon in previous studies,^{10,12,14,15} while we saw the efficiency of krypton increase less rapidly than xenon.

As a final observation, we see that the efficiency gap between the two gases is the smallest at the high-current 300 V and 20 A condition. A similar decrease in the efficiency gap with current density has been previously observed on unshielded thrusters.¹³ This trend suggests that increasing the discharge current rather than the voltage is one potential method of closing the gap between xenon and krypton operation at high powers. We discuss this possibility in further detail in Sec. V.

B. Individual contributions to efficiency

To complement the global analysis from Sec. IV A, we present here probe-based measurements of the individual contributions to anode efficiency. These data provide insight into the factors that are driving trends in performance with power and gas choice. To this end, Fig. 9 shows the thrust-calculated and probe-calculated anode efficiencies as well as the efficiency breakdown for xenon performance at three operating conditions. The numerical values and uncertainties are reported in tabular form in the Appendix. Across all points, we see that the anode efficiencies as measured by the thrust and from the probe suite match to within 2.4%, with an uncertainty of $\pm 5\%$ – 6% on the probe-calculated efficiencies. The magnitudes of these results are consistent with previous measurements

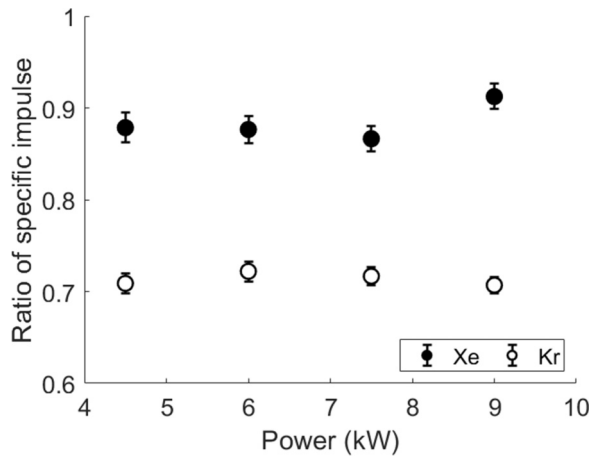


FIG. 8. Ratio of measured to theoretical limit of specific impulse for xenon and krypton at 15 A as a function of discharge power.

for a shielded Hall thruster operating in this range.¹⁸ In particular, the largest efficiency losses stem from the current utilization and divergence.

Figure 10 shows a breakdown of efficiency for krypton at the same operating conditions that we analyzed for xenon. The values and uncertainties are also reported in the Appendix. The difference between thrust-calculated and probe-calculated anode efficiencies match to within 2.1% with an uncertainty of $\pm 4\%$ – 7% on the probe-calculated values. As can be seen from Fig. 10 and as is

consistent with previous studies of unshielded thrusters operating on krypton,¹² the largest losses are in the current utilization, divergence, and mass utilization efficiencies. Of these, the largest difference from xenon is in the mass utilization. This loss likely stems from the higher ionization energy of krypton compared to xenon.^{12–15,17} We discuss this trend and its implication in more detail in Sec. V.

In summary, in this section, we have reported what is to our knowledge the first detailed comparison of the performance of a magnetically shielded Hall thruster operating on xenon vs krypton. We ultimately have found, consistent with earlier work on unshielded thrusters, that the efficiency when operating on krypton is lower. We similarly have shown from an analysis of the phenomenological efficiencies that the main contributor to the efficiency difference stems from the mass utilization. This is also consistent with previous work reported on unshielded thrusters. In comparing the performance gap between these propellants on shielded vs unshielded thrusters, we have found that the overall difference in efficiency remains approximately the same (5%–15% for US vs 9%–18% for MS). However, the trend in this gap differs, as the discrepancy between xenon and krypton efficiency decreases at higher voltages on unshielded thrusters^{10,12,14,15} while we observed the opposite trend in our experiment. In Sec. V, we elaborate on the differences between xenon and krypton performance and discuss potential reasons for the behavior at high voltages on unshielded and shielded thrusters.

V. DISCUSSION

In this section, we first discuss potential drivers for the observed trends in anode efficiency with varying voltage and current. We then examine possible physical mechanisms underlying the difference in

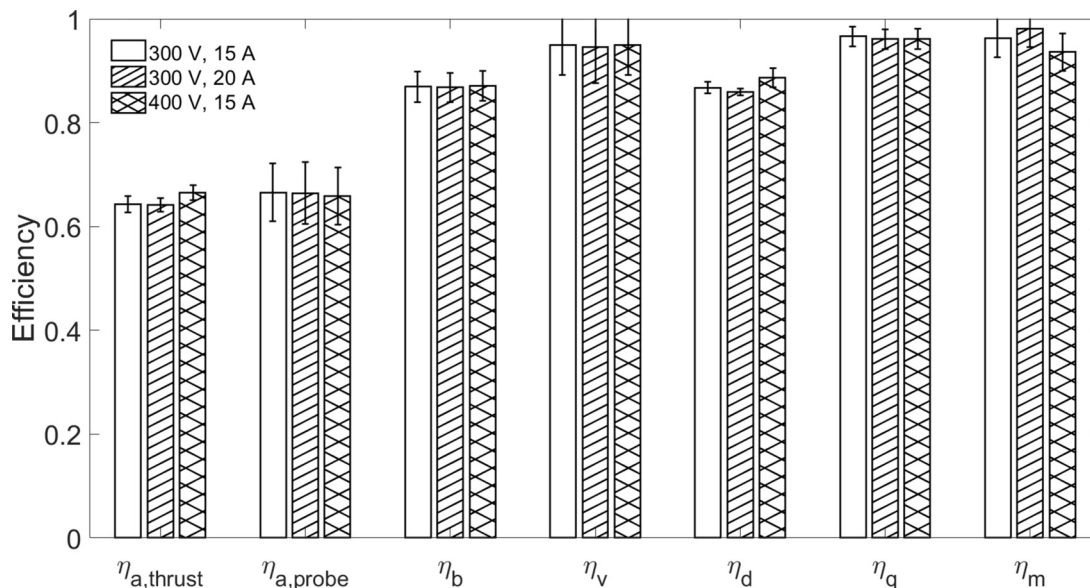


FIG. 9. Measurements of the contributions to anode efficiency for xenon inferred from far-field probes.

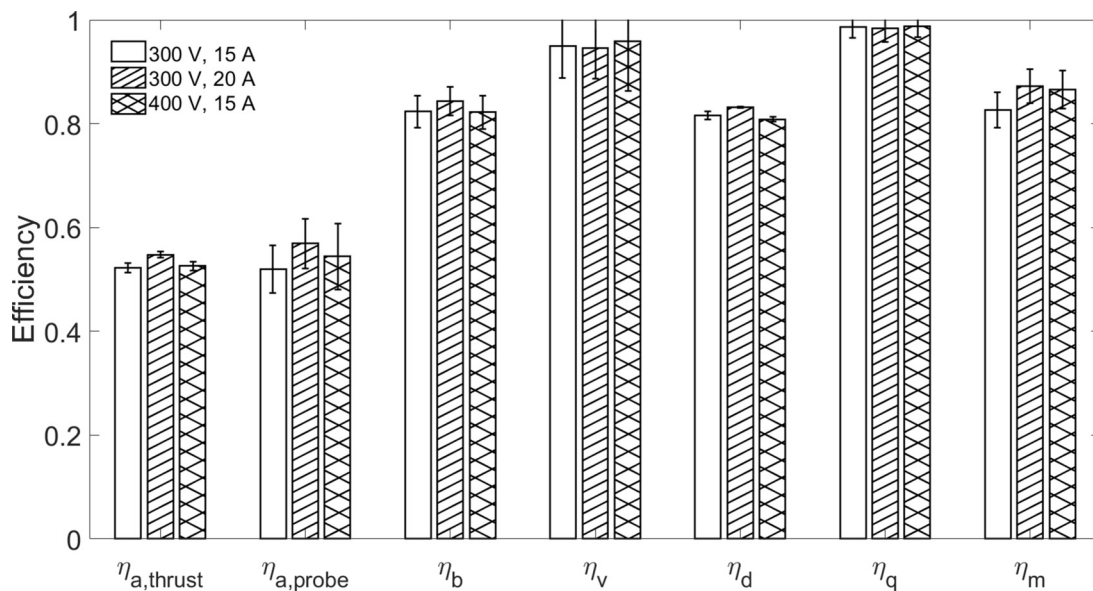


FIG. 10. Measurements of the contributions to anode efficiency for krypton inferred from far-field probes.

various efficiency modes between xenon and krypton, as well as how and why the trends may differ from unshielded thrusters. Finally, we leverage our findings to comment on strategies for improving the performance of a magnetically shielded Hall thruster operating on krypton.

A. Trends in anode efficiency with voltage and current

As noted in Sec. IV, the anode efficiency as a function of voltage increases for both gases [Fig. 7(c)]. Since our efficiency analyses of individual contributions (Figs. 9 and 10) do not extend to voltages higher than 400 V, we cannot explicitly point to the dominant drivers for this increase. Moreover, we see only minor changes in each efficiency mode (i.e., within uncertainty) between 300 and 400 V. Qualitatively, however, we can draw upon previous studies of unshielded thrusters to explain physically why our efficiencies increase with voltage.^{19,46} These studies have suggested that both current and mass utilization increase with voltage. The reason underlying the former trend is not well-understood; this stems from the fact that beam utilization is linked to electron mobility within the channel, which is non-classical and poorly understood in these devices.⁴⁷ The latter trend in mass utilization can be explained in part by the higher electron temperatures that occur at higher voltages, leading to improved ionization rates.⁴⁸

A notable behavior we see on the H9 that matches what has been previously observed on unshielded Hall thrusters is the improvement in krypton efficiency with current density.^{13–16} One study has attributed krypton's higher efficiencies at high-current densities to increases in the mass utilization, current utilization, and beam divergence.¹³ Although we only have two conditions to compare, these are the same three efficiencies for which we see the

gap between xenon and krypton close when comparing the 300 V, 15 A condition to the 300 V, 20 A condition (Fig. 11). Additionally, as seen in Fig. 7(c), the anode efficiency of krypton at the 20 A condition is 54.8%, the highest observed for krypton; at 600 V, 15 A, we measured an anode efficiency of 54.7% for krypton. One interesting difference between xenon and krypton is the manner in which the plume divergence changes with current and voltage. For xenon, the divergence efficiency primarily increases with increasing voltage, while for krypton, it primarily increases with increasing current. This behavior may point us toward potential optimization strategies for krypton operation on shielded thrusters.

B. Comparison of xenon and krypton operation

We look in this section to the three conditions for which we have probe data to help elucidate major drivers for the gap in efficiency between xenon and krypton. To this end, we show in Fig. 11 the differences between the two gases at each condition, $\Delta\eta = \eta_{Xe} - \eta_{Kr}$. Positive values indicate that the xenon efficiency is higher than that of krypton, while the reverse is true for negative values. As we discussed qualitatively in Sec. IV, the efficiency where krypton shows the largest disparity from xenon is the mass utilization, where the gap ranges from 7% to 14% with an uncertainty of about $\pm 5\%$ for all three conditions. The current and divergence efficiencies also contribute to the gap between xenon and krypton, with $\Delta\eta_b$ ranging from 2% to 5% with an uncertainty of about $\pm 4\%$ and $\Delta\eta_d$ ranging from 3% to 8% with an uncertainty of $\pm 1-2\%$.

The difference in mass utilization can be explained by the smaller ionization cross section of krypton compared to xenon. In the range of typical electron temperatures along centerline in the channel of a Hall thruster (typically 27–45 eV),¹⁸ the cross section

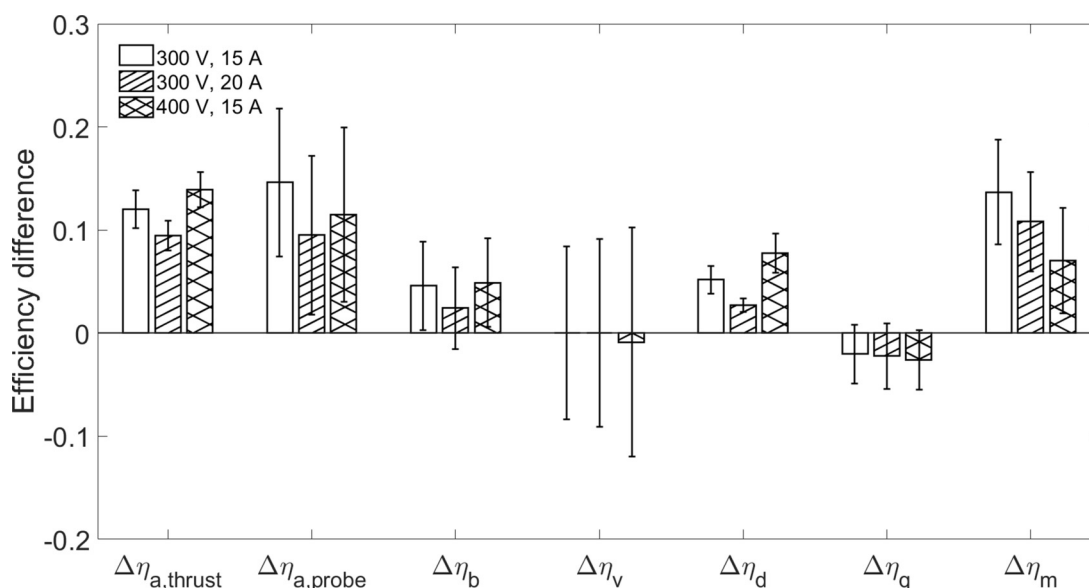


FIG. 11. Differences in the contributions to anode efficiency between krypton and xenon.

of xenon is 1.2–1.6 times larger than that of krypton.⁴⁸ As the ionization rate scales with this ionization cross section, the resultant mass utilization efficiency of krypton is lower.^{10,13,19} We expand upon this discussion in Sec. V C.

The second-highest driver of the lower krypton efficiency is the divergence. This is likely due to differences in the location of the acceleration region, defined as the narrow axial length over which the majority of the ions are accelerated. An acceleration region located further downstream of the exit plane is more curved, therefore contributing to divergence losses in the beam as ions can be accelerated radially as well axially.^{18,49} It has previously been shown that on an unshielded Hall thruster, the acceleration region moves downstream for krypton relative to xenon.⁵⁰ On an MS thruster, the peak of the acceleration zone is usually displaced slightly downstream compared to US thrusters as a result of the magnetic field geometry.¹⁸ Further downstream movement of this region, assuming the trend for krypton on US thrusters remains the same for MS thrusters, would only exacerbate this efficiency loss.

Finally, the third highest difference between the two propellants is in beam utilization efficiency. Low beam current utilization is an indication of reduced electron confinement.²² Our result, therefore, suggests that the electron mobility may be higher for krypton operation than it is for xenon, increasing the electron current in the channel [see Eq. (4)]. As electron transport in Hall thrusters is still a poorly understood phenomenon,⁴⁷ we are limited in our speculation of why this difference in efficiency exists.

Krypton holds a slight advantage in charge utilization of 2%–3% with an uncertainty of about $\pm 3\%$ over xenon. This trend is unsurprising given the higher ionization energy for both singly and multiply charged states of krypton relative to xenon,⁵¹

resulting in a lower population of multiply charged ions for krypton operation. This higher charge utilization efficiency of krypton also matches results reported in previous studies of unshielded thrusters.^{13,19}

C. Comparison of trends in magnetically shielded and unshielded thrusters

We briefly mentioned in our presentation of the results in Sec. IV that we observed a widening gap in xenon and krypton efficiency at high voltages, contrary to what has been reported in previous studies of unshielded thrusters. We expand upon potential drivers of this difference here.

One important consideration is that there are factors beyond the change in magnetic field geometry that could lead to this difference. For example, a number of previous studies on unshielded thrusters were conducted in constant-density mode instead of constant-power mode; i.e., instead of matching current between xenon and krypton, they matched neutral density at the anode.^{15,19,50} Some of the data observed at various operating conditions on these thrusters may, therefore, be difficult to directly compare with our results. Additionally, there are a number of design differences beyond the shape of the magnetic field between the various thrusters from these previous studies and the one we present here. These include the dimensions of the channel, the position of the cathode used, and the sizing of the thruster. These features can influence the overall efficiency. For example, the dimensions of the channel impact electron confinement, affecting the current utilization, and the position of the cathode is tied to the coupling voltage, affecting the voltage utilization. The implication is thus that shielding may not be the only reason for the

larger efficiency gap observed at high voltages between krypton and xenon.

With that said, shielding ultimately may still be the driving contributing factor. This is due to the larger typical electron temperatures along channel centerline for shielded vs unshielded Hall thrusters.¹⁸ As the electron temperature in most Hall thrusters scales with discharge voltage ($V_d \propto T_e$)²² and this temperature directly impacts the ionization, we anticipate that the mass utilization in shielded and unshielded thrusters should respond differently to variations in voltage.

To motivate this explanation quantitatively, we first make the simplifying assumption that mass utilization is the dominant driver for the difference in efficiencies. This can be approximated to first order as the ratio of mass flux of created charge carriers through ionization to the influx of neutral mass through the anode,

$$\eta_m \approx \frac{AL_{iz}n_n n_i v_{te} \sigma_{iz}(T_e) m_i}{\dot{m}_a}, \quad (22)$$

where A is the channel cross-sectional area, L_{iz} is the length of the ionization zone, n_n is the average neutral density, n_i is the average plasma density, v_{te} is the average electron thermal velocity, $\sigma_{iz}(T_e)$ is the ionization cross section, which is a function of the electron temperature, and m_i denotes the atomic mass of the gas.

We recognize that we can define the anode mass flow as $\dot{m}_a = An_n v_{th} m_i$, where v_{th} is the thermal speed of the neutral gas entering from the anode. Similarly, assuming negligible losses from multiple charge states as well as negligible voltage utilization losses, we can relate the plasma density to the discharge current through the approximation $n_i \approx \frac{\eta_b I_d}{Aq\sqrt{2qV_d/m_i}}$. With this result, we find that the mass utilization efficiency scales as

$$\eta_m \approx \eta_b \left(\frac{L_{iz}}{A}\right) \left(\frac{I_d}{q^{3/2}}\right) \sqrt{\frac{T_e}{2T_n m_e V_d}} \sigma_{iz}(T_e) m_i, \quad (23)$$

$$\eta_m \approx c\eta_b \left(\frac{L_{iz}}{A}\right) \left(I_d \sqrt{\frac{T_e}{T_n V_d}}\right) \sigma_{iz}(T_e) m_i, \quad (24)$$

where T_n is the neutral temperature at the anode in Kelvin, m_e is the electron mass, c is a constant value, and electron temperature is expressed in units of energy. Physically, this result illustrates several key drivers for the mass utilization efficiency. For example, increasing the discharge current for fixed voltage leads to higher mass utilization because the higher flow introduces more charge carriers in the channel that facilitate ionization. This could in part explain the behavior we see with discharge current from Fig. 7(c). Similarly, increasing the length of the ionization zone, L_{iz} , by extending the channel can lead to increased ionization. This indeed is one of the strategies for improving the performance of krypton with unshielded thrusters.^{15,17} Finally, we see intuitively that for a hotter plasma (higher T_e) with a larger ionization cross section, σ_{iz} , the mass utilization improves.

To further examine the relationship between electron temperature and mass utilization, we can express the ratio of this latter

value for xenon and krypton as

$$\frac{\eta_{Xe}}{\eta_{Kr}} \approx \Gamma \left(\frac{\sigma_{iz}(T_e)|_{Xe}}{\sigma_{iz}(T_e)|_{Kr}} \right). \quad (25)$$

Here, we have made the strong assumption that the electron temperature is the same for krypton and xenon at the same discharge voltage and discharge current. We similarly have incorporated all constants including c , ionization lengths, beam utilization efficiencies, temperatures of the neutral gas, and mass ratio into a new non-dimensional parameter Γ . We treat Γ as only weakly dependent on voltage for this discussion. The resulting simplified expression in Eq. (25) underscores the intuitive result that the ratio of mass utilization depends on the ratio of cross sections for ionization.

To illustrate the dependence of this ratio on discharge voltage, we next invoke the empirical scaling law that electron temperature trends linearly with discharge voltage, $V_d \approx \beta T_e$, where $\beta < 1$ is a constant.²² For traditional, unshielded thrusters, $\beta \sim 0.1$, whereas for shielded thrusters, $\beta > 0.1$.¹⁸ This stems in part from the fact that shielding mitigates electron thermal losses to the channel walls, raising the internal temperature of the electrons. Applying these assumptions to Eq. (25), we can now express the ratio of efficiencies as

$$\frac{\eta_{Xe}}{\eta_{Kr}} \approx \Gamma \left(\frac{\sigma_{iz}(\beta V_d)|_{Xe}}{\sigma_{iz}(\beta V_d)|_{Kr}} \right). \quad (26)$$

To evaluate this expression as a function of discharge voltage, we retrieved ionization cross sections to generate these plots through the LXCat database: the Biagi, Hayashi, Puech, SIGLO, and TRINITY databases were used for xenon, and the Biagi, Morgan, and SIGLO databases used for krypton.⁴⁸ These cross sections are shown in Fig. 12. This plot indicates that overall, the ionization cross section for xenon is higher than krypton. Additionally, in both cases, the cross sections are non-linear

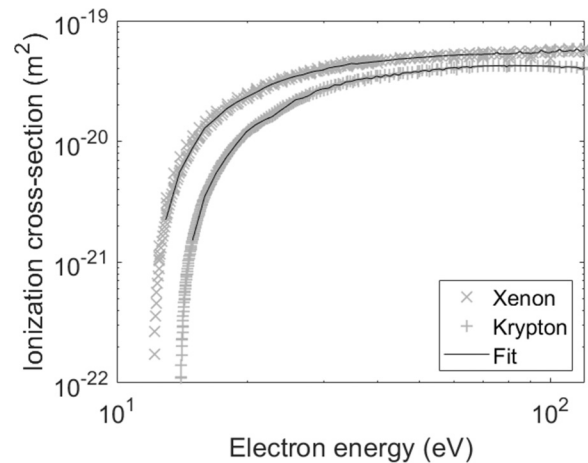


FIG. 12. Ionization cross sections for xenon and krypton as a function of electron energy. Values for cross-sectional areas are taken from the LXCat database⁴⁸ and fit with a linear piecewise polynomial.

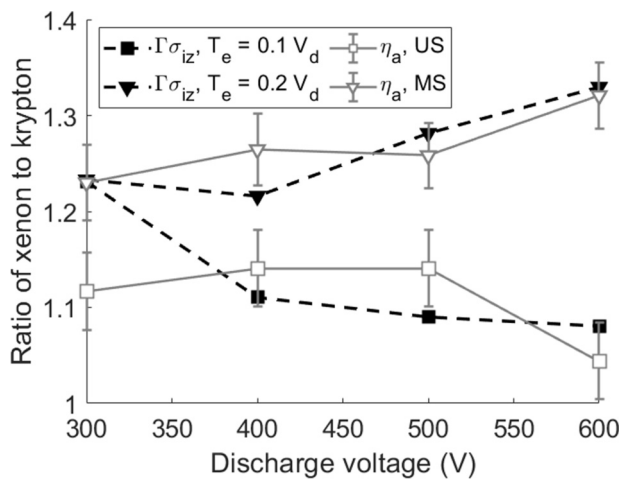


FIG. 13. Ratio between anode efficiency of xenon and krypton from scaling law [Eq. (26)] and from experimental results for shielded and unshielded thrusters (Ref. 14). The ratio between electron temperature and the discharge voltage is assumed to be 0.1 for the US case and 0.2 for the MS case. The values of Γ have been adjusted to best match the experimental data: $\Gamma = 0.85$ for the $\beta = 0.1$ case and $\Gamma = 0.97$ for the $\beta = 0.2$ case.

functions of temperature—the change in cross section becomes less sensitive with increasing energy.

We use these cross sections along with the expression in Eq. (26) to plot in Fig. 13 a comparison of the ratio of mass utilization efficiency as a function of discharge voltage for two values of β . We also show our measured ratio of anode efficiencies for our shielded thruster as well as a trend extracted from a study of an unshielded thruster operating at the same voltages from Ref. 14. We have adjusted Γ in each case to best qualitatively match the experimental datasets, assuming that the $\beta = 0.1$ case maps to the US condition and the $\beta = 0.2$ case maps to the MS condition.

From this plot, we see that when we assume the electron temperature to be $0.1 \times$ that of V_d ($\beta = 0.1$), the ratio of xenon to krypton efficiency decreases with voltage. However, for $\beta = 0.2$, this ratio increases from 300 to 600 V, indicating a widening gap in efficiency. Qualitatively, these scaling law results are consistent with experimental observations of efficiency ratio on unshielded and shielded thrusters. This agreement indicates that it is the higher temperatures in shielded thrusters for a given voltage and the fact that the ionization cross sections are nonlinear functions of temperature that may explain the change in efficiency gap with increasing discharge voltage between shielded and unshielded thrusters.

D. Strategies for optimizing performance on krypton

Our results from Fig. 11 indicate that the largest gaps between xenon and krypton efficiency are in mass utilization, beam utilization, and divergence. Improving these efficiencies is, therefore, the critical driver for krypton to become competitive with xenon as a high-performance Hall thruster propellant. We discuss in this section potential strategies for increasing the efficiency of each of these contributors.

In order to increase the beam utilization efficiency, it is ultimately necessary to reduce the electron current in these devices. However, as we have remarked previously, the processes driving electron current remain poorly understood.⁴⁷ It is, therefore, difficult to determine why this discrepancy exists and in turn strategies to mitigate it. With that being said, electron current typically is reduced in these devices by adjusting the magnetic field strength. In our study, we adjusted the magnetic field to minimize discharge oscillation strength at each set point. This minimum is not always coincident with the minimum in electron current.²¹ There is then potentially some margin for optimizing the magnitude of the magnetic field to reduce beam utilization losses.

The challenges with improving divergence efficiency mirror those with beam utilization. Indeed, since the beam divergence is linked with the location of the acceleration zone, which in turn is tied to the electron dynamics, it is difficult to identify physics-based strategies for closing this gap. We do note, however, that recent work has shown that increasing the cathode flow fraction has the effect of pushing the acceleration zone upstream in the thruster, thereby lowering divergence losses.^{52,53} This behavior potentially recommends a strategy for closing this efficiency gap on a krypton thruster, although operationally, the increase in cathode flux will represent a new overall efficiency loss to the thruster.

One established method for improving mass utilization is to extend channel length, therefore increasing the residence time for ionization.^{15,17} The theoretical justification for this approach is illustrated in Eq. (24) where we see a linear dependence on L_{iz} . We note, however, that this technique may not have the same degree of efficacy on shielded thrusters compared to unshielded thrusters. This stems from the fact that the magnetic shielding topology results in a downward shift of the plasma discharge with respect to the thruster exit plane. The ionization zone can, therefore, partially extend downstream of the channel. Increasing the channel length on a shielded thruster ultimately may not have as pronounced of an impact on improving ionization.

In addition to changing geometry, based on our results in Figs. 7(d) and 11, we see that the efficiency gap for krypton and xenon appears to close at the high-current condition. Equation (24) offers a justification for this behavior: as discharge current density I_d/A increases, the mass utilization efficiency is also expected to increase. This suggests that at sufficiently high currents, the entire mass flux will be ionized, ultimately closing the dominant driver of the efficiency gap between krypton and xenon.

To this point, our recent work has shown that with increasing current density on the H9 thruster operating on xenon, the mass utilization efficiency does ultimately approach unity.⁵⁴ Operationally, in order to maintain the same power levels while increasing current density, thrusters could be redesigned to have a smaller cross-sectional area. This could, however, invite challenges related to enhanced wall losses and overheating. On the other hand, current density can also be increased by operating at higher powers on a device of the same size. Indeed, at the high-power levels (>100 kW) required for crewed deep-space missions,^{55–57} it is possible that the mass utilization efficiency gap will close between xenon and krypton, making this latter gas an attractive alternative for these higher-power missions.

One final comment on the operation of a magnetically shielded Hall thruster on krypton is regarding the high oscillations

seen at high voltages. At 500 V, we observed oscillations of 160% in the discharge current, and this increased to 210% at 600 V. While we do not yet have conclusive strategies to dampen these oscillations, it is a critical factor to consider for thruster health when operating these devices on krypton at high voltages.

VI. CONCLUSION

In this work, we have measured global performance metrics and the various contributions to anode efficiency of xenon and krypton at discharge voltages ranging from 300 to 600 V and discharge currents of 15 and 20 A on a 9-kW class magnetically shielded Hall thruster. We have found that xenon operation reached a maximum anode efficiency of $72.3 \pm 1.4\%$ at 600 V and 15 A, while krypton reached a maximum anode efficiency of $54.8 \pm 0.8\%$ at 300 V and 20 A. We have shown that generally, the anode efficiency of krypton was worse than that of xenon at the same condition by 9%–18% with an uncertainty of 2%–3%. This gap is in family with the 5%–15% that has been observed from previous studies of krypton operation on unshielded thrusters.

We have discussed potential physical causes underlying the trends in our global performance parameters. As the discharge voltage increased, so did the acceleration voltage and the electron temperatures along centerline, improving the voltage and mass utilization. This resulted in the improved efficiencies seen at higher voltages. The specific impulse was improved by the higher acceleration voltages as well. For increasing current at a fixed discharge voltage, we saw higher thrust due to the higher anode flow rate and an improvement in anode efficiency due to the improved mass utilization at high-current densities for both propellants.

We contextualized these trends in anode efficiency by using far-field probe data to evaluate the major efficiency terms for the thruster operating at 300 and 400 V. From these results, we identified mass utilization as the primary detractor to krypton performance in comparison with xenon. This behavior also matches what has been seen on previous studies of unshielded thrusters. While our analysis ultimately showed that the efficiency gap between krypton and xenon was the same (within uncertainty) for US and MS thrusters, we did find one key difference at high voltages. Where the efficiency gap between xenon and krypton closed at high voltages for US thrusters, we saw this gap increase. We have discussed this result in the context of mass utilization efficiency, the major driver of the gap between krypton and xenon performance. In particular, we have shown that allowing for the fact that electron temperatures in MS thrusters are typically higher than US thrusters, the nonlinearity of the xenon and krypton ionization cross sections with temperature will lead to diverging behavior for US and MS thrusters.

Finally, we have discussed potential strategies for closing the efficiency gap between krypton and xenon operation on magnetically shielded Hall thrusters. These include changes to design and operation that address the specific efficiencies where krypton is worse than xenon, namely, in mass utilization, beam utilization, and divergence. Some of the proposed strategies for improving krypton performance include increasing the magnetic field strength, increasing cathode flow fraction, lengthening the thruster channel, and operating at higher current densities.

In summary, we have shown in this work that an MS thruster optimized for xenon can operate on krypton at the expense of a reduction in performance. This behavior ultimately does not represent a significant departure from the conclusions reached on previous studies of unshielded thrusters. The presence of magnetic shielding thus does not introduce evidently new or unexplained behavior. With that said, our comprehensive analysis in this work of the factors driving these efficiency trends can be leveraged to improve future designs and iterations of magnetically shielded, krypton-operated Hall thrusters. This may enable a new paradigm of higher-power, longer-lifetime thrusters operating on this attractive, alternative propellant.

ACKNOWLEDGMENTS

This work was supported by the Graduate Research Fellowship Program from the National Science Foundation (NSF). The authors would like to thank Dr. Ethan Dale, Matthew Byrne, and Zachariah Brown for their assistance in testing and data collection, Eric Vigés for his support in facility operation, and Dr. Richard Hofer from the Jet Propulsion Laboratory for fruitful discussions on Hall thruster testing and analysis.

AUTHOR DECLARATIONS

Conflict of Interest

The authors have no conflicts to disclose.

DATA AVAILABILITY

The data that support the findings of this study are available within the article.

APPENDIX: PERFORMANCE AND EFFICIENCY DATA

Xenon performance measurements (Table III). Krypton performance measurements (Table IV). Contributions to xenon efficiency

TABLE III. Xenon performance measurements.

Condition	Thrust (mN)	Isp (s)	η_a (%)	η_{tot} (%)
300 V, 15 A	292.9 ± 3.5	1881 ± 35	64.2 ± 1.6	58.6 ± 1.8
300 V, 20 A	377.6 ± 3.8	1944 ± 29	64.2 ± 1.3	58.9 ± 1.5
400 V, 15 A	350.8 ± 3.4	2168 ± 36	66.5 ± 1.5	61.0 ± 1.8
500 V, 15 A	405.1 ± 3.4	2395 ± 37	67.9 ± 1.4	62.5 ± 1.7
600 V, 15 A	447.2 ± 3.0	2763 ± 42	72.3 ± 1.4	66.5 ± 1.8

TABLE IV. Krypton performance measurements.

Condition	Thrust (mN)	Isp (s)	η_a (%)	η_{tot} (%)
300 V, 15 A	235.8 ± 2.5	1900 ± 29	52.2 ± 1.1	47.6 ± 1.3
300 V, 20 A	317.3 ± 2.0	1974 ± 21	54.8 ± 0.8	50.4 ± 1.0
400 V, 15 A	269.1 ± 2.5	2235 ± 33	52.6 ± 1.1	47.9 ± 1.2
500 V, 15 A	311.0 ± 2.2	2480 ± 33	54.0 ± 1.0	49.4 ± 1.2
600 V, 15 A	350.3 ± 2.5	2680 ± 35	54.7 ± 0.9	50.3 ± 1.1

TABLE V. Contributions to xenon efficiency inferred from probe measurements.

Condition	$\eta_{a,thrust}$	$\eta_{a,probe}$	η_b	η_v	η_d	η_q	η_m
300 V, 15 A	64.2 ± 1.6	66.6 ± 5.3	86.9 ± 3.0	94.9 ± 5.2	86.7 ± 1.1	96.6 ± 1.9	96.3 ± 3.8
300 V, 20 A	64.2 ± 1.3	66.4 ± 6.1	86.8 ± 2.8	94.6 ± 7.0	85.9 ± 0.7	96.1 ± 1.9	98.1 ± 3.5
400 V, 15 A	66.5 ± 1.5	65.9 ± 5.6	87.1 ± 2.9	94.9 ± 5.8	88.6 ± 1.8	96.1 ± 2.0	93.6 ± 3.6

TABLE VI. Contributions to krypton efficiency inferred from probe measurements.

Condition	$\eta_{a,thrust}$	$\eta_{a,probe}$	η_b	η_v	η_d	η_q	η_m
300 V, 15 A	52.2 ± 1.1	52.0 ± 4.6	82.3 ± 3.1	94.9 ± 6.2	81.6 ± 0.8	98.6 ± 2.2	82.6 ± 3.4
300 V, 20 A	54.8 ± 0.8	56.9 ± 4.7	84.3 ± 2.8	94.6 ± 5.7	83.2 ± 0.1	98.3 ± 2.6	87.2 ± 3.3
400 V, 15 A	52.6 ± 1.1	54.4 ± 6.1	82.2 ± 3.2	95.8 ± 8.9	80.9 ± 0.4	98.8 ± 2.1	$86. \pm 3.7$

inferred from probe measurements (Table V). Contributions to krypton efficiency inferred from probe measurements (Table VI).

REFERENCES

- G. Mikellides, I. Katz, R. R. Hofer, and D. M. Goebel, "Magnetic shielding of a laboratory Hall thruster. I. Theory and validation," *J. Appl. Phys.* **115**, 043303 (2014).
- R. R. Hofer, D. M. Goebel, I. G. Mikellides, and I. Katz, "Magnetic shielding of a laboratory Hall thruster. II. Experiments," *J. Appl. Phys.* **115**, 043304 (2014).
- R. P. Welle, "Xenon and krypton availability for electric propulsion—An updated assessment," in *29th Joint Propulsion Conference and Exhibit* (American Institute of Aeronautics and Astronautics, El Segundo, CA, 1993).
- T. Kokan and C. R. Joyner, "Mission comparison of Hall effect and gridded ion thrusters utilizing various propellant options," in *AIAA SPACE Conference and Exposition* (American Institute of Aeronautics and Astronautics, 2012).
- D. A. Herman and K. G. Unfried, "Xenon acquisition strategies for high power electric propulsion NASA missions," in *62nd JANNAF Propulsion Meeting* (Joint Army Navy NASA Air Force, Nashville, TN, 2015).
- V. Giannetti, T. Andreussi, A. Leporini, S. Gregucci, M. Saravia, A. Rossodivita, M. Andrenucci, D. Estublier, and C. Edwards, "Electric propulsion system trade-off analysis based on alternative propellant selection," in *Space Propulsion Conference*, series and number 1 (Rome, 2016).
- D. Lide, *Handbook of Chemistry and Physics*, 79th ed. (CRC Press, 1998).
- W. A. Hargus, L. J. Tango, and M. R. Nakles, "Background pressure effects on krypton Hall effect thruster internal acceleration," in *International Electric Propulsion Conference* (Electric Rocket Propulsion Society, Washington, D.C., 2013).
- R. P. Welle, "Propellant storage considerations for electric propulsion," in *International Electric Propulsion Conference* (Electric Rocket Propulsion Society, Viareggio, 1991).
- A. I. Bugrova, A. M. Bishaev, A. V. Desyatskov, M. V. Kozintseva, A. S. Lipatov, and M. Dudeck, "Experimental investigations of a krypton stationary plasma thruster," *Int. J. Aerosp. Eng.* **2013**, 1 (2013).
- J. Kurzyna, M. Jakubczak, A. Szelecka, and K. Dannenmayer, "Performance tests of IPPLM's krypton Hall thruster," *Laser Part. Beams* **36**, 105–114 (2018).
- R. R. Hofer, P. Y. Peterson, D. T. Jacobson, and D. M. Manzella, "Factors affecting the efficiency of krypton Hall thrusters," in *46th Meeting of the APS Division of Plasma Physics* (American Physical Society, Savannah, GA, 2004).
- J. A. Linnell and A. D. Gallimore, "Efficiency analysis of a Hall thruster operating with krypton and xenon," *J. Propul. Power* **22**, 1402–1418 (2006).
- H. Kamhawi, T. Haag, D. Jacobson, and D. Manzella, "Performance Evaluation of the NASA-300M 20 kW Hall thruster," in *47th Joint Propulsion Conference and Exhibit* (American Institute of Aeronautics and Astronautics, San Diego, CA, 2011).
- P. Peterson, D. Jacobson, D. Manzella, and J. John, "The performance and wear characterization of a high-power high-Isp NASA Hall thruster," in *41st Joint Propulsion Conference and Exhibit* (American Institute of Aeronautics and Astronautics, Tucson, AZ, 2005).
- C. Marrese, A. D. Gallimore, J. Haas, J. Foster, B. King, S. W. Kim, and S. Khartov, "An investigation of stationary plasma thruster performance with krypton propellant," in *31st Joint Propulsion Conference and Exhibit* (American Institute of Aeronautics and Astronautics, 1995).
- D. T. Jacobson and D. H. Manzella, "50 kW class krypton Hall thruster performance," in *39th Joint Propulsion Conference and Exhibit* (NASA, Huntsville, AL, 2003).
- R. Hofer, D. Goebel, I. Mikellides, and I. Katz, "Design of a laboratory Hall thruster with magnetically shielded channel walls, Phase II: Experiments," in *48th Joint Propulsion Conference and Exhibit* (American Institute of Aeronautics and Astronautics, Atlanta, GA, 2012).
- R. R. Hofer and A. D. Gallimore, "Efficiency analysis of a high-specific impulse Hall thruster," in *40th Joint Propulsion Conference* (American Institute of Aeronautics and Astronautics, Ft. Lauderdale, FL, 2004).
- R. Hofer, I. Katz, D. Goebel, K. Jameson, R. Sullivan, L. Johnson, and I. Mikellides, "Efficacy of electron mobility models in hybrid-PIC Hall thruster simulations," in *44th Joint Propulsion Conference and Exhibit* (American Institute of Aeronautics and Astronautics, Hartford, CT, 2008).
- R. R. Hofer, "Development and characterization of high-efficiency, high-specific impulse xenon Hall thrusters," Ph.D. thesis (University of Michigan, 2004).
- D. M. Goebel and I. Katz, in *Fundamentals of Electric Propulsion: Ion and Hall Thrusters*, edited by J. H. Yuen (Jet Propulsion Laboratory, California Institute of Technology, Pasadena, CA, 2008).
- R. R. Hofer, S. E. Cusson, R. B. Lobbia, and A. D. Gallimore, "The H9 magnetically shielded Hall thruster," in *35th International Electric Propulsion Conference* (Electric Rocket Propulsion Society, Atlanta, GA, 2017).
- S. E. Cusson, R. R. Hofer, R. Lobbia, B. A. Jorns, and A. D. Gallimore, "Performance of the H9 magnetically shielded Hall thrusters," in *35th International Electric Propulsion Conference* (Electric Rocket Propulsion Society, Atlanta, Georgia, 2017).
- R. R. Hofer, D. M. Goebel, and R. M. Walker, "Compact Lab6 hollow cathode for a 6-kW Hall thruster," in *54th JANNAF Propulsion Meeting* (Joint Army Navy NASA Air Force, 2018), pp. 14–17.
- P. Y. Peterson, H. Kamhawi, W. Huang, J. Yim, D. Herman, G. Williams, J. Gilland, and R. Hofer, "NASA HERMeS Hall thruster electrical configuration

- characterization,” in *52nd Joint Propulsion Conference* (American Institute of Aeronautics and Astronautics, 2016).
- ²⁷E. A. Vigas, B. A. Jorns, A. D. Gallimore, and J. P. Sheehan, “University of Michigan’s upgraded Large Vacuum Test Facility,” in *36th International Electric Propulsion Conference* (Electric Rocket Propulsion Society, Vienna, 2019).
- ²⁸J. W. Dankanich, M. Walker, M. W. Swiatek, and J. T. Yim, “Recommended practice for pressure measurement and calculation of effective pumping speed in electric propulsion testing,” *J. Propul. Power* **33**, 668–680 (2017).
- ²⁹S. E. Cusson, R. R. Hofer, D. M. Goebel, M. P. Georgin, A. R. Vazsonyi, B. A. Jorns, A. D. Gallimore, and I. D. Boyd, “Development of a 30-kW class magnetically shielded nested Hall thruster,” in *36th International Electric Propulsion Conference* (Electric Rocket Propulsion Society, Vienna, 2019).
- ³⁰K. G. Xu and M. L. Walker, “High-power, null-type, inverted pendulum thrust stand,” *Rev. Sci. Instrum.* **80**, 055103 (2009).
- ³¹J. P. Sheehan, Y. Raitse, N. Hershkowitz, and M. McDonald, “Recommended practice for use of emissive probes in electric propulsion testing,” *J. Propul. Power* **33**, 614–637 (2017).
- ³²R. B. Lobbia and B. E. Beal, “Recommended practice for use of Langmuir probes in electric propulsion testing,” *J. Propul. Power* **33**, 566–581 (2017).
- ³³B. Efron and R. J. Tibshirani, *An Introduction to the Bootstrap* (CRC Press, 1994).
- ³⁴W. Huang, R. Shastry, G. C. Soulas, and H. Kamhawi, “Farfield plume measurement and analysis on the NASA-300M and NASA-300MS,” in *33rd International Electric Propulsion Conference* (Electric Rocket Propulsion Society, Washington, D.C., 2013).
- ³⁵R. Shastry, R. R. Hofer, B. M. Reid, and A. D. Gallimore, “Method for analyzing $E \times B$ probe spectra from Hall thruster plumes,” *Rev. Sci. Instrum.* **80**, 063502 (2009).
- ³⁶W. Huang and R. Shastry, “Analysis of Wien filter spectra from Hall thruster plumes,” *Rev. Sci. Instrum.* **86**, 073502 (2015).
- ³⁷J. S. Miller, S. H. Pullins, D. J. Levandier, Y. H. Chiu, and R. A. Dressler, “Xenon charge exchange cross sections for electrostatic thruster models,” *J. Appl. Phys.* **91**, 984–991 (2002).
- ³⁸M. L. Hause, B. D. Prince, and R. J. Bemish, “Krypton charge exchange cross sections for Hall effect thruster models,” *J. Appl. Phys.* **113**, 163301 (2013).
- ³⁹D. L. Brown, M. L. Walker, J. Szabo, W. Huang, and J. E. Foster, “Recommended practice for use of Faraday probes in electric propulsion testing,” *J. Propul. Power* **33**, 582–613 (2017).
- ⁴⁰H. D. Hagstrum, “Auger ejection of electrons from molybdenum by noble gas ions,” *Phys. Rev.* **104**, 672 (1956).
- ⁴¹H. D. Hagstrum, “Auger ejection of electrons from tungsten by noble gas ions,” *Phys. Rev.* **96**, 325 (1954).
- ⁴²J. M. Haas, “Low-perturbation interrogation of the internal and near-field plasma structure of a Hall thruster using a high-speed probe positioning system,” Ph.D. thesis (University of Michigan, Ann Arbor, 2001).
- ⁴³W. Huang, H. Kamhawi, and T. Haag, “Facility effect characterization test of NASA’s HERMeS Hall thruster,” in *52nd Joint Propulsion Conference* (American Institute of Aeronautics and Astronautics, Salt Lake City, UT, 2016).
- ⁴⁴D. L. Brown and A. D. Gallimore, “Evaluation of facility effects on ion migration in a Hall thruster plume,” *J. Propul. Power* **27**, 573–585 (2011).
- ⁴⁵R. R. Hofer and A. D. Gallimore, “Recent results from internal and very-near-field plasma diagnostics of a high specific impulse Hall thruster,” in *28th International Electric Propulsion Conference* (Electric Rocket Propulsion Society, Toulouse, France, 2003).
- ⁴⁶D. L. Brown, C. W. Larson, B. E. Beal, and A. D. Gallimore, “Methodology and historical perspective of a Hall thruster efficiency analysis,” *J. Propul. Power* **25**, 1163–1177 (2009).
- ⁴⁷J. P. Boeuf, “Tutorial: Physics and modeling of Hall thrusters,” *J. Appl. Phys.* **121**, 011101 (2017).
- ⁴⁸M. C. Bordage, S. F. Biagi, L. L. Alves, K. Bartschat, S. Chowdhury, L. C. Pitchford, G. J. Hagelaar, W. L. Morgan, V. Puech, and O. Zatsarinnny, “Comparisons of sets of electron-neutral scattering cross sections and swarm parameters in noble gases: III. Krypton and xenon,” *J. Phys. D* **46**, 334003 (2013).
- ⁴⁹S. E. Cusson, E. T. Dale, B. A. Jorns, and A. D. Gallimore, “Acceleration region dynamics in a magnetically shielded Hall thruster,” *Phys. Plasmas* **26**, 023506 (2019).
- ⁵⁰J. A. Linnell and A. D. Gallimore, “Internal plasma potential measurements of a Hall thruster using xenon and krypton propellant,” *Phys. Plasmas* **13**, 093502 (2006).
- ⁵¹J. A. R. Samson and R. B. Cairns, “Ionization potential of molecular xenon and krypton,” *J. Opt. Soc. Am.* **56**, 1140–1141 (1966).
- ⁵²D. M. Goebel, K. K. Jameson, and R. R. Hofer, “Hall thruster cathode flow impact on coupling voltage and cathode life,” *J. Propul. Power* **28**, 355–363 (2012).
- ⁵³S. E. Cusson, M. P. Byrne, B. A. Jorns, and A. D. Gallimore, “Investigation into the use of cathode flow fraction to mitigate pressure-related facility effects on a magnetically shielded Hall thruster,” in *Propulsion and Energy Forum* (American Institute of Aeronautics and Astronautics, 2019).
- ⁵⁴L. L. Su and B. A. Jorns, “Performance at high current densities of a magnetically-shielded Hall thruster,” in *Propulsion and Energy Forum* (American Institute of Aeronautics and Astronautics, 2021).
- ⁵⁵R. Myers and C. Carpenter, “High power solar electric propulsion for human space exploration architectures,” in *32nd International Electric Propulsion Conference* (Electric Rocket Propulsion Society, Wiesbaden, Germany, 2011).
- ⁵⁶R. Myers, C. Joyner, R. Cassady, S. Overton, T. Kokan, H. Horton, and W. Hoskins, “Affordable exploration architectures using the space launch system and high power solar electric propulsion,” in *34th International Electric Propulsion Conference* (Electric Rocket Propulsion Society, Kobe, Japan, 2015).
- ⁵⁷National Academies of Sciences, Engineering, and Medicine, “Space nuclear propulsion for human mars exploration,” Technical Report (The National Academies Press, Washington, D.C., 2021).